Nagaoka spin-valley ordering in silicene quantum dots

Piotr Jurkowski and Bartłomiej Szafran

AGH University of Science and Technology, Faculty of Physics and Applied Computer Science, al. Mickiewicza 30, 30-059 Kraków, Poland

(Received 24 December 2020; revised 22 February 2021; accepted 15 March 2021; published 23 March 2021)

We study a cluster of quantum dots defined within silicene that hosts confined electron states with spin and valley degrees of freedom. Atomistic tight-binding and continuum Dirac approximations are applied for a few-electron system in the quest for spontaneous valley polarization driven by interdot tunneling and an electron-electron interaction, i.e., a valley counterpart of itinerant Nagaoka ferromagnetic ordering recently identified in a GaAs square cluster of quantum dots with three excess electrons [J. P. Dehollain *et al.*, Nature (London) **579**, 528 (2020)]. We find that for a Hamiltonian without intrinsic spin-orbit coupling the valley polarization in the ground state can be observed in a range of interdot spacings provided that the spin of the system is frozen by an external magnetic field. The intervalley scattering effects are negligible for a cluster geometry that supports the valley-polarized ground state. In the presence of a strong intrinsic spin-orbit coupling that is characteristic to silicene, no external magnetic field is necessary for the observation of a ground state that is polarized in both the spin and valley. The effective magnetic field due to the spin-orbit interaction produces a perfect anticorrelation of the spin and valley isospin components in the low-energy spectrum. Experimental detection of spin-valley ground-state polarization by a charge response to a potential variation is discussed.

DOI: 10.1103/PhysRevB.103.125306

I. INTRODUCTION

The Hubbard model for a cubic lattice with an on-site Coulomb interaction dominating over the intersite hopping produces a spin-polarized ground state near half filling [1] that is known as Nagaoka ferromagnetism in the theory of itinerant ferromagnetism [2]. Semiconductor quantum dots were pointed out as a possible two-dimensional (2D) realization of the Hubbard model and artificial molecules or clusters formed by multiple quantum dots were studied in the context of spin polarization driven by interdot tunneling and an electron-electron interaction [3,4]. A spin-ordered ground state was recently experimentally identified in electrostatic quantum dots defined in GaAs [5] in a three-electron system for quantum dots arranged in a square cluster, a case previously theoretically studied in Ref. [3].

In graphene [6] and 2D xenes [7] the electron states near the charge neutrality point are additionally characterized by a valley isospin due to the presence of two nonequivalent Dirac points in the Brillouin zone. Electrostatic confinement in graphene is excluded by the Klein tunneling effect [8]. However, in bilayer graphene [9,10] or buckled silicene [11] the energy gap and thus electrostatic confinement can be formed by a perpendicular electric field.

In this paper we look for a counterpart of the Nagaoka ferromagnetism in the valley degree of freedom in a 2D system. We focus on the ground-state valley polarization for a three-electron system in a square cluster of quantum dots defined in silicene [7], i.e., a counterpart of the case studied experimentally in a GaAs system [5]. With respect to the III-V quantum dots the silicene besides the valley degree of freedom hosts a strong intrinsic spin-orbit coupling [12,13], which as we show below plays a role in the Nagaoka ordering. Without the spin-orbit coupling term the tight-binding Hamiltonian is identical with the one for monolayer graphene with a staggered potential [14–16] up to the numerical value of the interatomic hopping energy. For that reason below we solve both problems with and without spin-orbit coupling. We demonstrate that in the absence of spin-orbit coupling the spin degree of freedom of the three-electron system needs to be frozen for the valley ordering to be observed. The intrinsic spin-orbit coupling splits the fourfold degeneracy of the confined single-electron ground state with respect to the spin and valley forming spin-valley doublets in a manner similar to the one closely studied for carbon nanotubes [17]. We demonstrate that in the presence of intrinsic spin-orbit coupling, Nagaoka ordering in both the valley and spin appears simultaneously. We discuss the detection of spin-valley ordering by an electron charge reaction to the sweep of confinement potentials in the cluster. Nagaoka ordering of the valley can be added to the toolbox of valleytronics [18,19].

II. THEORY

Below, we study the system with the tight-binding approach [12,13,20] and with the continuum approximation [12,21] to the tight-binding Hamiltonian. The two approaches differ in the description of the valley degree of freedom, which is intrinsically included in the Hamiltonian only in the continuum version, that neglects the intervalley scattering by short-range defects, the edges [22] of the flake, and the short-range component of the electron-electron interaction potential [23–25]. The diagonalization of the tight-binding Hamiltonian for localized states covers the contribution of the

entire Brillouin zone to the confined states and the valley can only be resolved *a posteriori*. The atomistic method intrinsically accounts for the intervalley scattering. The application of the two methods allows for a resolution of the intervalley scattering effects. The continuum method, when applicable, provides a radical reduction of the numerical complexity with respect to the tight-binding (TB) approach. The latter takes in orbitals localized on each atom while the nodes in the finite element method (FEM) can be separated by much larger distances than depend only on the long-range wave-function variation, so that the continuum approach can be applied to arbitrarily large systems. However, due to the neglect of the intervalley scattering, the reliability of the FEM needs to be verified against the atomistic approach.

A. Atomistic tight-binding Hamiltonian

For the TB model we define a flake of buckled silicene [20,26] with ions of the A sublattice at positions $\mathbf{r}_{\mathbf{k}}^{A} = k_1\mathbf{a}_1 + k_2\mathbf{a}_2$ with the crystal lattice vectors $\mathbf{a}_1 = a(\frac{1}{2}, \frac{\sqrt{3}}{2}, 0)$, and $\mathbf{a}_2 = a(1, 0, 0)$, with a silicene lattice constant $a = 3.89$ Å. The B sublattice is shifted by a base vector $\mathbf{r}_{\mathbf{k}}^{B} = \mathbf{r}_{\mathbf{k}}^{A} + (0, d, \delta)$ where $d = 2.25$ Å is the in-plane nearest-neighbor distance and the vertical distance is denoted by $\delta = 0.46$ Å. Calculations are performed for a hexagonal flake with armchair edges and a side length of about 30 nm with approximately 72 000 p_z spin orbitals.

We determine the eigenstates of the atomistic TB Hamiltonian [12,13,20],

$$H_{\mathrm{TB}} = -t\sum_{\langle k,l\rangle} p_{kl}c_k^{\dagger}c_l + \sum_k V_k c_k^{\dagger}c_k + it_{\mathrm{SO}}\sigma_z \sum_{\langle\langle k,l\rangle\rangle} p_{kl}\nu_{kl}c_k^{\dagger}c_l + \frac{g\mu_B}{2}\vec{\sigma}\cdot\mathbf{B}, \qquad (1)$$

where the first sum describes the nearest-neighbor hopping with the energy $t = 1.6$ eV [12,13]. In Eq. (1), $p_{kl} = \exp\left(i\frac{e}{\hbar}\int_{\vec{r}_k}^{\vec{r}_l}\vec{\mathbf{A}}\cdot\vec{dl}\right)$ stands for the Peierls phase. The integral in the exponent of p_{kl} accounts for the Aharonov-Bohm phase shifts that the wave functions acquire from the vector potential $\mathbf{A}$ via hopping. We consider the magnetic field with both perpendicular B_z and in-plane B_x components $\mathbf{B} = (B_x, 0, B_z)$ with the vector potential $\mathbf{A} = (-B_z y/2, B_z x/2 - B_x z, 0)$. Due to the 2D nature of the material the in-plane component does not produce noticeable orbital effects. The in-plane field is introduced in order to manipulate spins of the confined states via the spin Zeeman effect included in the last term in Eq. (1), with μ_B as the Bohr magneton and $g = 2$ as the Landé factor. The third sum in Eq. (1) introduces the intrinsic spin-orbit interaction [27] with the coupling constant $t_{\mathrm{SO}} = 3.9$ meV [12,13] and $\nu_{kl} = +1$ (-1) for the path of the next-nearest-neighbor hopping from ion l to k via the common neighbor that turns counterclockwise (clockwise). The second sum in Eq. (1) introduces the external potential with V_k standing for the potential on the $\mathbf{r}_k$ ion.

In silicene the bias between sublattices opens the energy gap in the band structure [11] that allows for the formation of the confinement potential. For the confinement potential we assume that the bias is independent of the electron position within the plane,

$$V_k = \begin{cases} -V_g\sum_{i=1}^{4}\left[\exp\left(-r_{ik}^2/R^2\right) - 1\right] \text{ on A}, \\ -V_g\sum_{i=1}^{4}\left[\exp\left(-r_{ik}^2/R^2\right) + 1\right] \text{ on B}, \end{cases} \qquad (2)$$

where the sum over i runs over four quantum dots with centers $\mathbf{g}_i$ and $\mathbf{r}_{ik} = |\mathbf{r}_k - \mathbf{g}_i|$. We take $R = 4.2$ nm for the dot radius, and $V_g = 0.3$ eV for the depth of the potential cavities. In Eq. (2) the electrostatic potential is lowered on both sublattices near the center of each quantum dot. This type of potential variation—with nearly equal bias and a minimum on both sublattices—can be achieved with a pair of flat gate electrodes with one that contains a circular intrusion near the quantum dot center [28]. Note that type I quantum dots can also be produced with flat gates provided that they contain apertures near the confinement area [29].

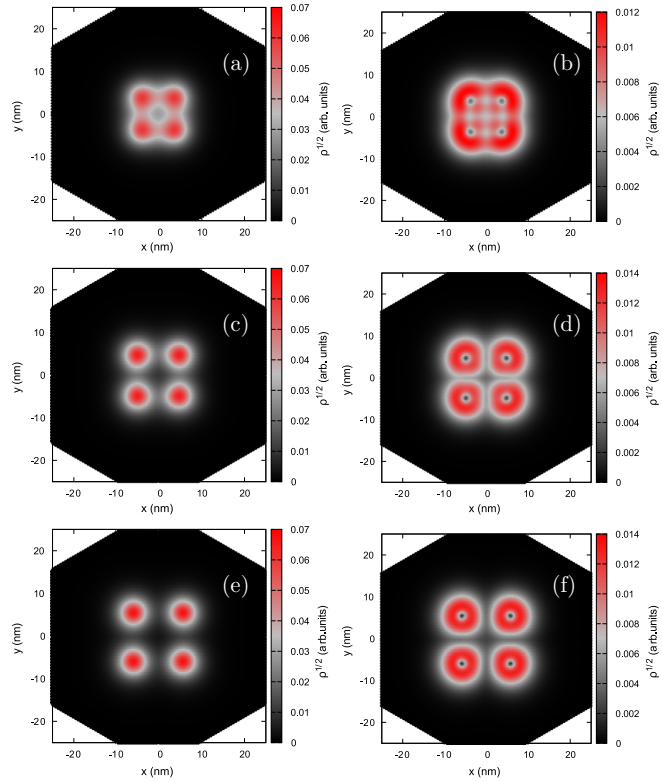

FIG. 1. Square root of the charge density of the three-electron ground states as calculated with the TB for a neglected spin-orbit interaction. The left (right) panels indicate the electron densities in the A (B) sublattice. The rows of figures from top to bottom correspond to centers of the quantum dots placed on the corners of a square with side (a), (b) 8.4 nm, (c), (d) 10 nm, and (e), (f) 11.7 nm.

Three-electron charge densities for the centers of the quantum dots $\mathbf{g}_i$ forming a square of side length X are given in Fig. 1 with the A (B) sublattice placed on the left (right) column of plots, and the side of the square increasing from top to bottom.

B. Continuum Hamiltonian

The continuum approximation explicitly resolves the valley degree of freedom. We work with a four-component wave function spanned on sublattice and spin subspaces $\psi =$

$(\psi^{A\uparrow}\ \psi^{B\uparrow}\ \psi^{A\downarrow}\ \psi^{B\downarrow})^T$, and the energy operator [12,21]

$$H = \left[\hbar v_F(k_x\tau_x - \eta k_y\tau_y) + \begin{pmatrix} V_A(\mathbf{r}) & 0 \\ 0 & V_B(\mathbf{r}) \end{pmatrix}\right] \otimes \mathbf{I}_{\text{spin}} + \eta t_{\text{SO}}\tau_z \otimes \sigma_z + \mathbf{I}_{\text{sublattice}} \otimes \frac{g\mu_B}{2}\vec{\sigma}\cdot\mathbf{B} - W_D\nabla^2\tau_z \otimes \mathbf{I}_{\text{spin}}, \tag{3}$$

where σ and τ are the Pauli matrices in the spin and sublattice subspaces, respectively. $\mathbf{I}_{\text{sublattice}}$ and $\mathbf{I}_{\text{spin}}$ are the identity matrices, and the Fermi velocity is $v_F = 3dt/2\hbar$. The wave-vector operators are defined as $\mathbf{k} = -i\nabla + \frac{e}{\hbar}\mathbf{A}$, and $\eta = \pm 1$ is the valley index.

Hamiltonian (3) is diagonalized by the FEM. The computational box is divided typically into about 2200 triangular elements with 18 000 nodes supporting Lagrange interpolating polynomials of the second degree [30] as shape functions covering the spin and sublattice spaces. In Eq. (3) the last expression is an artificial Wilson term [31] that is applied to remove the spurious states [31–34] due to the fermion doubling problem from the low-energy spectrum. We take the Wilson parameter $W_D = 36$ meV nm^2 which increases the energy of the fast oscillating states with a negligible influence on the actual solutions of the Dirac equation that are smooth near the charge neutrality point.

C. Calculations for three electrons

The electron-electron interaction for gapless graphene flakes leads to the generation of electron and hole pairs [35]. In the calculations that follow for the three-electron system the typical total interaction energy is about 60 meV, i.e., $\simeq$20 meV per electron pair, i.e., much lower than the potential bias between the sublattices. Since the interaction energy is lower than the field-induced energy gap and the considered quantum dot does not support the confinement of holes, we neglect the effects of pair generation by the Coulomb interaction [35] and assume that the number of conduction band electrons is fixed [36]. In both the atomistic method and in FEM we diagonalize the Hamiltonian in the basis of three-electron wave functions constructed by the lowest-energy 48 confined eigenstates of the conduction band that produces the basis of 17 296 Slater determinants.

The Hamiltonian for a system of interacting electrons is

$$H_i = \sum_i d_i^\dagger d_i E_i + \frac{1}{2}\sum_{ijkl} d_i^\dagger d_j^\dagger d_k d_l V_{ijkl}, \tag{4}$$

where $d_i^\dagger$ is the electron creation operator for the energy level E_i. The two-electron Coulomb matrix elements are

$$V_{ijkl} = \kappa\langle\psi_i(\mathbf{1})\psi_j(\mathbf{2})|\frac{1}{|\mathbf{r_{12}}|}|\psi_k(\mathbf{1})\psi_l(\mathbf{2})\rangle, \tag{5}$$

with $\kappa = e^2/(4\pi\epsilon\epsilon_0)$. We take $\epsilon_0 = 4.5$ for the dielectric constant, that corresponds to SiO_2 or thin layers of Al_2O_3 [37,38] applied as a matrix embedding the silicene monolayer.

1. Coulomb integrals in the continuum approach

For the continuum approach we calculate the Coulomb matrix elements using the formula

$$\begin{aligned} V_{ijkl} = \kappa\delta_{\eta_i,\eta_k}\delta_{\eta_j,\eta_l}\iint d\mathbf{r}_1 d\mathbf{r}_2 \big[&\psi_i^{A\uparrow *}(\mathbf{r}_1)\psi_k^{A\uparrow}(\mathbf{r}_1) \\ &+ \psi_i^{B\uparrow *}(\mathbf{r}_1)\psi_k^{B\uparrow}(\mathbf{r}_1) + \psi_i^{A\downarrow *}(\mathbf{r}_1)\psi_k^{A\downarrow}(\mathbf{r}_1) \\ &+ \psi_i^{B\downarrow *}(\mathbf{r}_1)\psi_k^{B\downarrow}(\mathbf{r}_1)\big]\frac{1}{|\mathbf{r}_{12}|}\big[\psi_j^{A\uparrow *}(\mathbf{r}_2)\psi_l^{A\uparrow}(\mathbf{r}_2) \\ &+ \psi_j^{B\uparrow *}(\mathbf{r}_2)\psi_l^{B\uparrow}(\mathbf{r}_2) + \psi_j^{A\downarrow *}(\mathbf{r}_2)\psi_l^{A\downarrow}(\mathbf{r}_2) \\ &+ \psi_j^{B\downarrow *}(\mathbf{r}_2)\psi_l^{B\downarrow}(\mathbf{r}_2)\big]. \end{aligned} \tag{6}$$

The deltas with the valley indices that stand before the integral imply the neglect of the intervalley scattering effects [23–25] that are accounted for only in the TB approach.

2. Coulomb integrals in the atomistic approach

In the TB method the single-electron wave functions ψ are expanded in the basis of $3p_z$ spin orbitals of Si ions,

$$\psi_i(\mathbf{r}_i) = \sum_{k,\sigma_k} C^i_{k,\sigma_k} p_z^k(\mathbf{r}_1). \tag{7}$$

The Coulomb matrix elements are summed over the ions,

$$\begin{aligned} V_{ijkl} = \kappa \sum_{\substack{a,\sigma_a;b,\sigma_b;\\ c,\sigma_c;d,\sigma_d}} &C^{i*}_{a,\sigma_a} C^{j*}_{b,\sigma_b} C^{k}_{c,\sigma_c} C^{l}_{d,\sigma_d} \delta_{\sigma_a;\sigma_d}\delta_{\sigma_b;\sigma_c} \\ &\times \langle p_z^a(\mathbf{r}_1)p_z^b(\mathbf{r}_2)|\frac{1}{|r_{12}|}|p_z^c(\mathbf{r}_1)p_z^d(\mathbf{r}_2)\rangle. \end{aligned} \tag{8}$$

In the two-center approximation [36] $\langle p_z^a(\mathbf{r}_1)p_z^b(\mathbf{r}_2)|\frac{1}{|r_{12}|}|p_z^c(\mathbf{r}_1)p_z^d(\mathbf{r}_2)\rangle = \frac{1}{r_{ab}}\delta_{ac}\delta_{bd}$ for $a \neq b$. The on-site integral ($a = b$) for $3p_z$ Si atomic orbitals with $p_z(\mathbf{r}) = Nz(1 - \frac{Zr}{6})\exp(-Zr/3)$, where N stands for the normalization and Z is the effective screened nucleus charge, equals $\frac{3577}{46080}Z$. The Slater screening rules for $3p$ Si orbitals give $Z = 4.15$.

III. RESULTS AND DISCUSSION

A. Single-dot, single-electron results

In the absence of a spin-orbit interaction and without an external magnetic field the single-electron confined ground state in a single quantum dot is fourfold degenerate with respect to both spin and valley [Fig. 2(a)]. For $B_z = 0$ the valley degeneracy is preserved for the in-plane field B_x and the energy levels are split only with respect to the spin. In Fig. 2(b) and in other plots of this work presented as functions of B_x we apply a residual perpendicular magnetic field for $B_z = 10$ mT which lifts the degeneracies of the energy levels to a thickness of a line.

The intrinsic spin-orbit coupling introduces an effective magnetic field perpendicular to the plane of confinement with an orientation that is opposite in the sense of the eigenvalue sign to the valley isospin η [cf. the term with the t_{SO} coupling constant in Eq. (3)]. This effective field splits [Fig. 2(c)] the ground state into a pair of doublets with a splitting energy that corresponds to the spin Zeeman effect at a magnetic field as

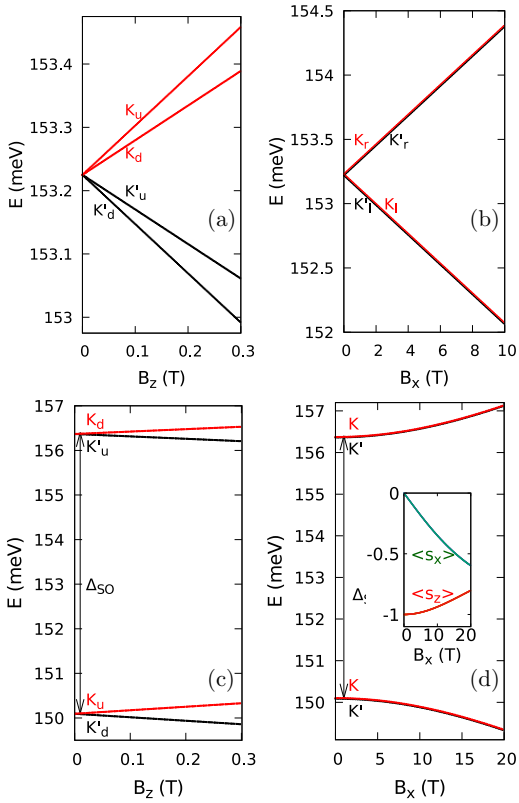

FIG. 2. Low-energy single-electron spectrum of states confined in a *single* quantum dot (a), (b) without and (c), (d) with the spin-orbit interaction. The results in (a) and (c) are obtained for $B_x = 0$ and in (b) and (d) for $B_z = 10$ mT. The subscripts u/d in (a) and (c) correspond to spin-up and spin-down eigenstates of the σ_z operator. In (b), l and r subscripts stand for the eigenstates of the σ_x operator with negative and positive eigenvalues, respectively. The inset in (d) shows the average values of the σ_x and σ_z operators for the ground state.

large as ∼34 T. The application of an in-plane magnetic field [Fig. 2(d)] slowly tilts the spins to the x direction [see the inset in Fig. 2(d)].

B. Three electrons in a quadruple quantum dot for $t_{SO} = 0$

For a single circular quantum dot the single-electron ground state corresponds to an angular momentum quantum number 0 for the wave-function component on sublattice A and ±1 on sublattice B [28]. In consequence, the charge density in a single quantum dot corresponds to a maximum and a zero of the charge density in the centers of the quantum dots on the A and B sublattice, respectively. The single-electron properties are consistent with the charge density distribution for three interacting electrons with well-separated wave functions—see Figs. 1(e) and 1(f) for the centers of potential minima distributed on a square with a side length of $X = 11.7$ nm. The wave-function component on the B sublattice is less strongly localized and thus it mediates the interdot tunneling to a stronger extent.

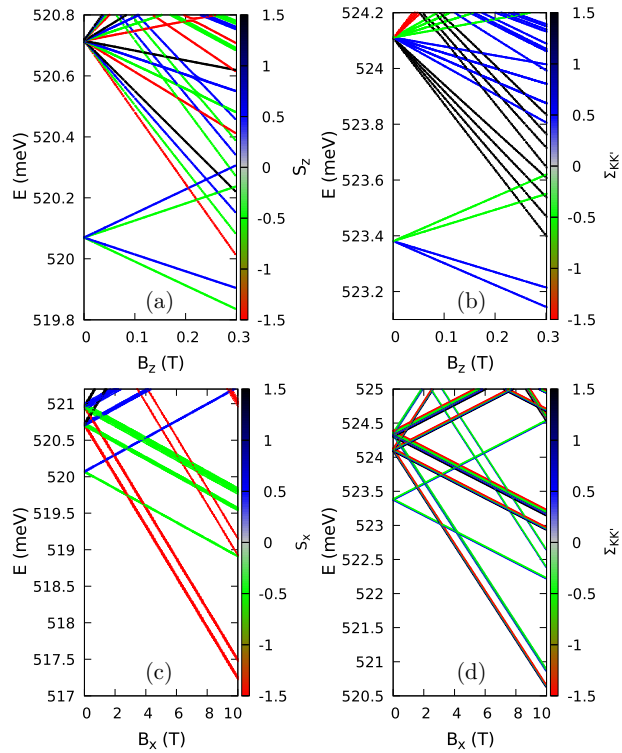

FIG. 3. Three-electron energy levels for the quadruple quantum dot as calculated within (a), (c) TB and (b), (d) FEM. The results in (a) and (c) are obtained for $B_x = 0$ and in (b) and (d) for $B_z = 10$ mT. The spin-orbit interaction is neglected ($t_{SO} = 0$). The color scale in (a), (c) and (b), (d) indicates the z component of the spin and the valley isospin component, respectively. The centers of the four quantum dots are placed on the corners of a square with a side length of $X = 11.7$ nm.

1. Nagaoka valley ordering

The three-electron spectrum is given in Fig. 3(a) (TB) and in Fig. 3(b) (FEM). The results of the two approaches agree very well up to a relative shift of the entire spectra on the energy scale of a few meV. In the results of the atomistic approach we plot the energy levels with colors indicating the total spin z or x component. On the energy levels calculated with FEM we mark by the color of the lines the total valley isospin component for the three electrons.

The three-electron ground state at $B_z = 0$ is fourfold degenerate. The degenerate energy levels correspond to the eigenvalue of the $S_z = \frac{1}{2}\sum_{i=1}^{3}\sigma_z^i$ component of the total spin $\pm\frac{1}{2}$ and the z component of the total valley isospin of $\Sigma_{KK'} = \frac{1}{2}\sum_{i=1}^{3}\eta_z^i$ equal to $\pm\frac{1}{2}$. The ground state is not polarized in either the spin or the valley. The first excited state is 16-fold degenerate. The energy levels that are degenerate at $B_z = 0$ correspond to the total valley index $\Sigma_{KK'} = -\frac{3}{2}, -\frac{1}{2}, \frac{1}{2}, \frac{3}{2}$ and the z components of the spin $S_z = -\frac{3}{2}, -\frac{1}{2}, \frac{1}{2}, \frac{3}{2}$.

Nagaoka ferromagnetism was observed [5] in a quadruple quantum dot defined in GaAs, with three electrons per eight available spin orbitals. In the silicene system we have 16 available spin-valley orbitals due to the additional valley degree of freedom. One can try to eliminate the spin degree of freedom and reduce the number of equivalent states to eight by

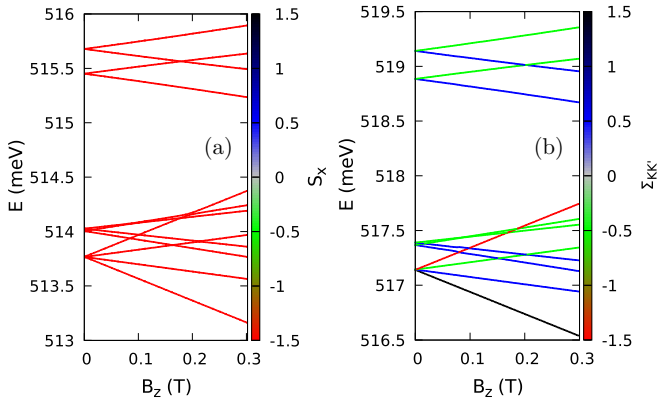

FIG. 4. Same as Figs. 3(a) and 3(b) only with an in-plane magnetic field $B_x = 20$ T. (a) shows the TB results and (b) the FEM ones. The centers of the four quantum dots are placed on the corners of a square with a side length of $X = 11.7$ nm and $t_{SO} = 0$.

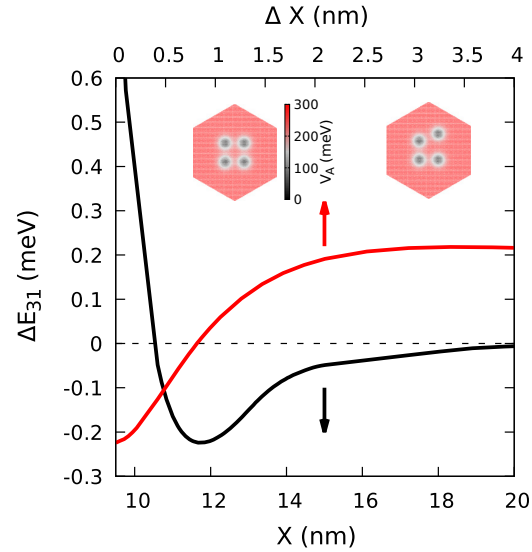

FIG. 5. The black lines show the energy difference (FEM) between the lowest valley-polarized and nonpolarized states for $B_x = 20$ T and $t_{SO} = 0$ as a function of the side length of a square on which the centers of the four quantum dots are placed. The red line shows the results obtained for $X = 11.7$ nm, which corresponds to the most stable valley-polarized ground state as a function of a shift Δx of the y position of the quantum dot localized in the first quadrant of the Cartesian coordinate. The insets show the potential on the A sublattice for $X = 11.7$ nm and $\Delta X = 0$ (left) and $\Delta X = 4$ nm (right). The same scale for V_A is applied for both sublattices. The frame in the insets has a length of 60 nm.

applying a strong magnetic field to freeze the spin degree of freedom. The application of the perpendicular magnetic field lifts the valley degeneracy [Fig. 2(a)] that would eventually lead to the valley polarization by the external field. Here, we want to preserve the valley degeneracy in order to study the electron-electron interaction triggering the valley polarization. For that reason we choose to apply the in-plane field that interacts only with the spin and not the valley of confined states [Fig. 2(b)]. The results are given in Figs. 3(c) and 3(d) with a residual $B_z = 10$ mT applied to slightly split the energy levels for visualization. The states that are spin polarized in the $-x$ direction for all valley configurations are promoted to the lower energy by the B_x field.

The structure of the low-energy spectrum spin polarized by a strong B_x field is revealed once a weak B_z field is additionally applied. In Fig. 4 we set $B_x = 20$ T and calculate the energy levels as functions of B_z. In the applied range of $B_z \leqslant 0.3$ T the spins remain nearly perfectly polarized in the $-x$ direction. The ground state at $B_z = 0$ is fourfold degenerate with the valley isospin component that takes values $-\frac{3}{2}$, $-\frac{1}{2}$, $\frac{1}{2}$, and $\frac{3}{2}$. This structure of the ground-state energy level is a valley-ordered counterpart of a spin-polarized three-electron state with a total spin quantum number $S = \frac{3}{2}$. In the excited part of the spectrum in Fig. 4 we find a number of valley nonpolarized states forming doublets at $B_z = 0$ with the valley isospin equal to $\pm\frac{1}{2}$. By analogy to the spin degree of freedom we attribute the total valley isospin quantum number $V = \frac{3}{2}$ to the fourfold-degenerate state with the isospin component $\Sigma_{KK'}$ changing from $-V$ to V with steps of 1. The doublets thus correspond to $V = \frac{1}{2}$ with the components $\Sigma_{KK'} = \pm\frac{1}{2}$.

The Nagaoka polarization of the ground state appears due to the interdot electron tunneling and thus it is determined by the system geometry. In order to study the valley polarization we kept $B_x = 20$ T and varied the positions of the centers of the dots. We define ΔE_{31} as the energy difference between the lowest valley-polarized state with $V = \frac{3}{2}$ and the lowest nonpolarized state with a $V = \frac{1}{2}$ state. $\Delta E_{31} < 0$ corresponds to the Nagaoka ordered valley in the ground state. The black line in Fig. 5 shows the result as a function of X—the side length of the square on which the centers of the dots are placed (Fig. 1).

The valley-polarized ground state is found for $X \gtrsim 10.5$ nm. The polarized ground state is most stable for $X = 11.7$ nm that was selected for plots in Figs. 1(e), 1(f) 3, and 4. For low values of X the four quantum dots become more strongly tunnel coupled and they eventually are transformed to a single quantum dot for which the ground state is not polarized. In the limit of large X the interdot tunneling is negligible. Once the electrons are separated and their hopping between the dots is removed, the valley isospin has no influence on the energy for $B_z = 0$, hence the degeneracy of $V = \frac{3}{2}$ and $V = \frac{1}{2}$ states at large X.

Reference [5] found that the ground-state spin ordering vanishes when the array of dots is deformed to approach the limit of a quantum dot chain. For a chain of dots [39] the Lieb-Mattis theorem [40,41] excludes spin polarization of the ground state. Here, we looked for a similar effect in the valley degree of freedom. We fixed the value of X to 11.7 nm and moved the quantum dot localized in the first quadrant of the coordinate system ($x > 0$, $y > 0$, see the insets in Fig. 5), shifting its center by ΔX in the y direction. The results are displayed in Fig. 5 by the red line. The shift by $\Delta X \simeq 0.75$ nm makes the valley-polarized and nonpolarized states degenerate. For $\Delta X \gtrsim 2.1$ nm the value of ΔE_{31} is more or less inverted from the $\Delta X = 0$ case.

2. Intervalley scattering effects

The intervalley scattering can appear as (i) a single-electron effect triggered by the armchair edge [22] of the

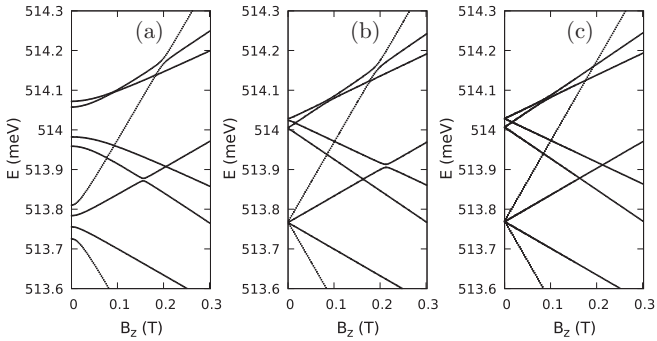

FIG. 6. Enlarged low-energy part of the spectra for parameters of Fig. 4 for the side length of the hexagonal silicene flake of length (a) 20.5 nm, (b) 23 nm, and (c) 25 nm as calculated with the atomistic method.

flake and (ii) as an interaction effect due to the short-range component of the Coulomb potential [23–25].

The effect (i) can be observed for a smaller flake, when the tails of quantum-dot-confined wave functions tunnel to the armchair edge that induces intervalley mixing. Figure 6 shows a zoom of the low part of the spectra for parameters applied in Fig. 4 with the side length of the flake of 20.5 nm [Fig. 6(a)], 23 nm [Fig. 6(b)], and 25 nm [Fig. 6(c)]. The valley mixing due to the edge effect lifts the degeneracy at $B_z = 0$ and opens avoided crossings between energy levels that in the continuum approach correspond to different valley isospin quantum numbers [compare with Fig. 4(b)]. For strong intervalley mixing the dependence of the energy levels of B_z deviates from linear, in particular near $B_z = 0$.

The effect (ii) is not triggered when the electrons occupy separate quantum dots. In this case only the long-range tail of the Coulomb potential is resolved by carriers.

In Fig. 7 we plotted the results for quantum dot centers placed at the corners of the square of side length $X = 10$ nm. For these parameters the valley ordering is no longer observed in the ground state (see Fig. 5). In Fig. 7 we can see that the agreement between the two methods is no longer as perfect as above. In particular, the valley-ordered quadruplet is found here only by the continuum approach but in the TB the

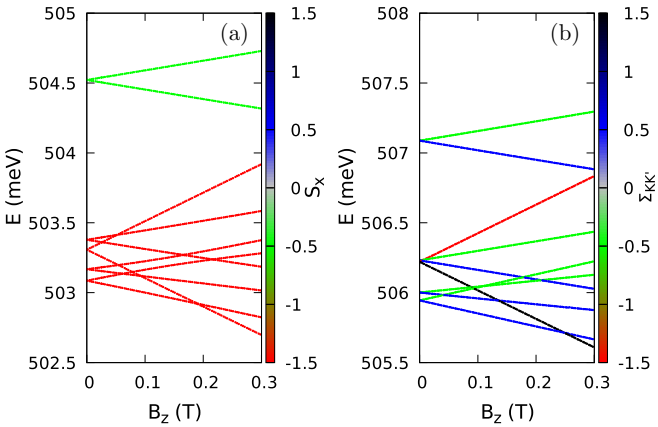

FIG. 7. Same as Fig. 4 only with the interdot distance decreased to $X = 10$ nm.

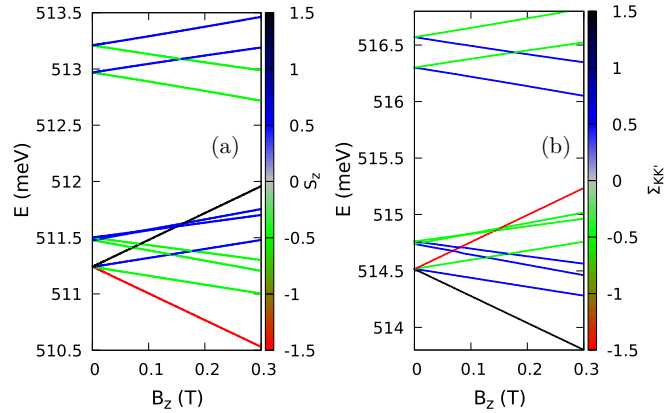

FIG. 8. Same as Fig. 4 only with $t_{SO} = 3.9$ meV, $B_x = 0$. The color scale in (a) now shows the z component of the spin.

quadruplet is split into two doublets. The two-electron levels splitting by the intervalley scattering due to the electron-electron interaction was discussed in detail in Ref. [28] for an electron pair in a single quantum dot [see Figs. 4(a) and 4(b) in Ref. [28]].

We conclude that, in the parameter range where Nagaoka ordering is found, the intervalley scattering by the Coulomb interaction is negligible or missing for a system geometry for which Nagaoka valley ordering appears.

C. Nagaoka polarization in the presence of a spin-orbit interaction

Figure 8 shows the spectra for $X = 11.7$ nm and $t_{SO} = 3.9$ meV in the absence of an in-plane field $B_x = 0$. The pattern of energy levels is similar to the one found in Fig. 4 for $t_{SO} = 0$ and $B_x = 20$ T. For $t_{SO} = 3.9$ meV and $B = 0$ a single dot hosts a twofold-degenerate ground state [Figs. 2(c) and 2(d)] with opposite spin and valley isospin components $\eta\sigma_z = -1$. This pattern of energy levels replaces the valley-degenerate ground state with $\eta = \pm 1$ found for $t_{SO} = 0$, $B_z = 0$, and a strong in-plane field that freezes the spin found for Fig. 2(b). In these two above cases the Coulomb integrals between the single-electron states in the low-energy part of the spectrum are similar, hence the agreement of the three-electron spectra in Figs. 8 and 4. In the presence of an intrinsic spin-orbit interaction there is a perfect anticorrelation between the S_z and $\Sigma_{KK'}$ quantum numbers [Figs. 8(a) and 8(b)]. All the information on the eigenstates is therefore redundantly included in the spin and valley sets of quantum numbers.

D. Detection of polarized states

The confined spectra including the low-energy excited states can be studied with the transport spectroscopy that was developed for GaAas quantum dots [42] and more recently applied to graphene quantum dots [43,44] or carbon nanotubes [17,45]. The spin-valley structure of the spectrum can be extracted from the degeneracy and slopes of the energy levels [17,46] in an external magnetic field that can be measured with a precision of several μeV [46]. Besides the energy level dependence on the external magnetic field, the detection of the ground-state spin polarization is performed in experiments

on multiple quantum dots using the confinement potential variation [5,47,48]. The confinement potential is first fixed for a time long enough for the electron system to relax to the ground state. Next, the potential undergoes a change [5,47,48] such that after the sweep the ground state corresponds to two electrons in one of the dots. The change is applied diabatically, i.e., faster than the spin or valley relaxation time. The ground state with a double occupancy of a quantum dot can only be occupied provided that initially the electrons are not polarized, otherwise the double occupancy is forbidden by Pauli exclusion (valley-spin blockade [45]). The charge of the dots is monitored by on-chip charge sensors [5,47,48].

For the study of charge redistribution we take the system considered in the preceding section and generalize the potential of Eq. (2) in order to cover the confinement variation,

$$V_k(\mathbf{r}_k) = \begin{cases} -V_g \sum_{i=1}^{4} \left[\exp\left(-r_{ik}^2/R^2 \right) - 1 \right]/\alpha_i \text{ on A}, \\ -V_g \sum_{i=1}^{4} \left[\exp\left(-r_{ik}^2/R^2 \right) + 1 \right]/\alpha_i \text{ on B}, \end{cases} \tag{9}$$

where we take $\alpha_i = \alpha$ for the three dots localized at $x < 0$ or $y < 0$ leaving $\alpha_i = 1$ for the dot of the first quadrant.

The charge localized in each quadrant for the lowest-energy spin-valley-polarized state and the lowest-energy unpolarized state for $B = 0$ are displayed in Fig. 9(a) as a function of α. The square of the charge density is plotted in Fig. 9(b). For $\alpha = 1$ we have 3/4 electron charge per quantum dot in both polarized and unpolarized states. A difference in the charge distribution can only appear when the potential symmetry is lifted. As α is increased from 1, the dots on the left-hand and lower side of the cluster are made shallower. The reaction of the charge in both the states is at first similar as α is increased from 1. The upper-right-hand dot captures an entire electron charge at the expense of the other dots. Moreover, the unpolarized state becomes the ground state for $\alpha \geqslant 1.028$. Polarization removal from the ground state is consistent with the results for the deformed cluster of dots (see Fig. 5). As α is increased further in the unpolarized state, a second electron starts to occupy the dot of the first quadrant and simultaneously the charge of the opposite dot is increased to minimize the interdot electron-electron interaction energy. A double occupancy of the dot is forbidden for the polarized state and its charge distribution does not change much when α is increased above 1.1. In order to detect the initial spin-valley polarization one needs to diabatically sweep α from 1 to, i.e., 2.5, and next measure the charge localized in the dot of the first quadrant. The procedure should also be useful for the determination of the spin and valley relaxation times.

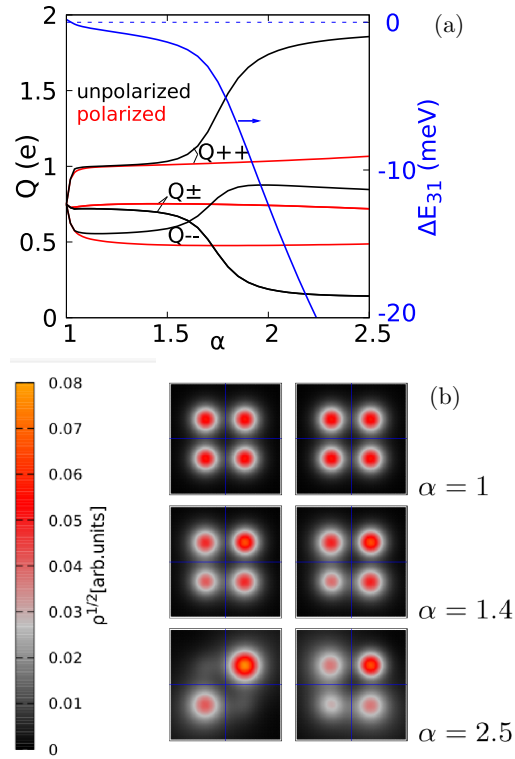

FIG. 9. (a) Charge localized in the upper-right-hand ($x > 0, y > 0$) quadrant ($Q++$), the lower-left-hand ($x < 0, y < 0$) quadrant $Q--$, and in the other quadrants $Q\pm$ ($x < 0, y > 0$) or ($x > 0, y < 0$), as a function of the divisor α which lowers the confinement potential in the left and lower quadrants $x < 0$ or $y < 0$ [see Eq. (2) for the lowest-energy spin-valley-polarized state (red lines) and the lowest-energy unpolarized state (black lines)]. The blue line shows the energy (FEM) difference between the polarized and unpolarized levels (ΔE_{31} right axis). (b) Square root of the charge density for the lowest polarized and unpolarized energy levels. The side of the each square plot is 34 nm long. Parameters are the same as in Sec. III C.

IV. SUMMARY AND CONCLUSIONS

We studied a system of three electrons in a square cluster of quantum dots defined within a material that provides a valley degree of freedom to the confined single-electron states using the continuum approach that allows for identification of the valley isospin in the atomistic TB spectra. We found that the Nagaoka-type polarization of the valley in a system without intrinsic spin-orbit coupling is found in conditions when the spin degree of freedom is frozen by an in-plane magnetic field. A nonpolarized ground state is promoted when the spatial symmetry of the cluster is lifted by a shift of one of the quantum dots that transforms the cluster toward a chain of quantum dots. In the presence of intrinsic spin-orbit coupling the spin-valley polarization is observed along with the perfect anticorrelation of the spin and valley isospin components already in the absence of an external magnetic field. The pattern of the energy levels near the ground state for systems with and without spin-orbit coupling is very similar provided that a strong in-plane magnetic field is applied to the latter. The spontaneous ground-state valley polarization in the system can be harnessed for studies of valley manipulation in multiple quantum dots. The Nagaoka valley polarization can be detected by charge conversion using the Pauli blockade of the double occupancy of a quantum dot.

ACKNOWLEDGMENTS

This work was supported by the National Science Centre (NCN) according to decision DEC-2016/23/B/ST3/00821. Calculations were performed on the PL-Grid infrastructure.

[1] Y. Nagaoka, Phys. Rev. **147**, 392 (1966).
[2] H. Tasaki, Prog. Theor. Phys. **99**, 489 (1998).
[3] D. C. Mattis, Int. J. Nanosci. **2**, 165 (2003).
[4] E. Nielsen and R. N. Bhatt, Phys. Rev. B **76**, 161202(R) (2007).
[5] J. P. Dehollain, U. Mukhopadhyay, V. P. Michal, Y. Wang, B. Wunsch, C. Reichl, W. Wegscheide, M. S. Rudner, E. Demler, and L. M. K. Vandersypen, Nature (London) **579**, 528 (2020).
[6] A. H. Castro Neto, F. Guinea, N. M. R. Peres, K. S. Novoselov, and A. K. Geim, Rev. Mod. Phys. **81**, 109 (2009).
[7] A. Molle, J. Goldberger, M. Houssa, Y. Xu, S.-C. Zhang, and D. Akinwande, Nat. Mater. **16**, 163 (2017).
[8] M. I. Katsnelson, K. S. Novoselov, and A. K. Geim, Nat. Phys. **2**, 620 (2006).
[9] E. V. Castro, K. S. Novoselov, S. V. Morozov, N. M. R. Peres, J. M. B. Lopes dos Santos, J. Nilsson, F. Guinea, A. K. Geim, and A. H. Castro Neto, Phys. Rev. Lett. **99**, 216802 (2007).
[10] J. M. Pereira, P. Vasilopulos, and F. M. Peeters, Nano Lett. **7**, 946 (2007).
[11] Z. Ni, Q. Liu, K. Tang, J. Zheng, J. Zhou, R. Qin, Z. Gao, D. Yu, and J. Lu, Nano Lett. **12**, 113 (2012).
[12] C.-C. Liu, W. Feng, and Y. Yao, Phys. Rev. Lett. **107**, 076802 (2011).
[13] M. Ezawa, Phys. Rev. Lett. **109**, 055502 (2012).
[14] J. Wurm, A. Rycerz, I. Adagideli, M. Wimmer, K. Richter, and H. U. Baranger, Phys. Rev. Lett. **102**, 056806 (2009).
[15] S. Schnez, K. Ensslin, M. Sigrist, and T. Ihn, Phys. Rev. B **78**, 195427 (2008).
[16] D. R. da Costa, A. Chaves, M. Zarenia, J. M. Pereira, Jr., G. A. Farias, and F. M. Peeters, Phys. Rev. B **89**, 075418 (2014).
[17] E. A. Laird, F. Kuemmeth, G. A. Steele, K. Grove-Rasmussen, J. Nygard, K. Flensberg, and L. P. Kouwenhoven, Rev. Mod. Phys. **87**, 703 (2015).
[18] J. R. Schaibley, H. Yu, G. Clark, P. Rivera, J. S. Ross, K. L. Seyler, W. Yao, and X. Xu, Nat. Rev. Mater. **1**, 16055 (2016).
[19] A. Rycerz, J. Tworzydło, and C. W. J. Beenakker, Nat. Phys. **3**, 172 (2007).
[20] S. Chowdhury and D. Jana, Rep. Prog. Phys. **79**, 126501 (2016).
[21] M. Ezawa, New J. Phys. **14**, 033003 (2012).
[22] M. Zarenia, A. Chaves, G. A. Farias, and F. M. Peeters, Phys. Rev. B **84**, 245403 (2011).
[23] L. Mayrhofera and M. Grifoni, Eur. Phys. J. B **63**, 43 (2008).
[24] A. Secchi and M. Rontani, Phys. Rev. B **88**, 125403 (2013).
[25] S. Pecker, F. Kuemmeth, A. Secchi, M. Rontani, D. C. Ralph, P. L. McEuen, and S. Ilani, Nat. Phys. **9**, 576 (2013).
[26] C.-C. Liu, H. Jiang, and Y. Yao, Phys. Rev. B **84**, 195430 (2011).
[27] C. L. Kane and E. J. Mele, Phys. Rev. Lett. **95**, 226801 (2005).
[28] B. Szafran and D. Zebrowski, Phys. Rev. B **98**, 155305 (2018).
[29] B. Szafran, D. Zebrowski, and A. Mrenca-Kolasinska, Sci. Rep. **8**, 7166 (2018).
[30] P. Solin, *Partial Differential Equations and the Finite Element Method* (Wiley, New York, 2005).
[31] Y. Tanimura, K. Hagino, and H. Z. Liang, Prog. Theor. Exp. Phys. **2015**, 073D01 (2015).
[32] K. G. Wilson, Phys. Rev. D **10**, 2445 (1974).
[33] L. Susskind, Phys. Rev. D **16**, 3031 (1977).
[34] F. Fillion-Gourdeau, E. Lorin, and A. D. Bandrauk, Comput. Phys. Commun. **183**, 1403 (2012).
[35] T. Paananen and R. Egger, Phys. Rev. B **84**, 155456 (2011).
[36] K. A. Guerrero-Becerra and M. Rontani, Phys. Rev. B **90**, 125446 (2014).
[37] H. Birey, J. Appl. Phys. **48**, 5209 (1977).
[38] M. D. Groner, J. W. Elam, F. H. Fabreguette, and S. M. George, Thin Sol. Films **413**, 186 (2002).
[39] B. Szafran, F. M. Peeters, S. Bednarek, T. Chwiej, and J. Adamowski, Phys. Rev. B **70**, 035401 (2004).
[40] E. Lieb and D. Mattis, Phys. Rev. **125**, 164 (1962).
[41] E. B. Kolomeisky and J. P. Straley, Rev. Mod. Phys. **68**, 175 (1996).
[42] R. Hanson, L. P. Kouwenhoven, J. R. Petta, S. Tarucha, and L. M. K. Vandersypen, Rev. Mod. Phys. **79**, 1217 (2007).
[43] M. Eich, F. Herman, R. Pisoni, H. Overweg, A. Kurzmann, Y. Lee, P. Rickhaus, K. Watanabe, T. Taniguchi, M. Sigrist, T. Ihn, and K. Ensslin, Phys. Rev. X **8**, 031023 (2018).
[44] J. Guettinger, F. Molitor, C. Stampfer, S. Schnez, A. Jacobsen, S. Droescher, T. Ihn, and K. Ensslin, Rep. Prog. Phys. **75**, 126502 (2012).
[45] F. Pei, E. A. Laird, G. A. Steele, and L. P. Kouenhoven, Nat. Nanotechnol. **7**, 630 (2012).
[46] F. Kuemmeth, S. Ilani, D. C. Ralp, and. P. L. McEuen, Nature (London) **452**, 448 (2008).
[47] B. M. Maune, M. G. Borselli, B. Huang, T. D. Ladd, P. W. Deelman, K. S. Holabird, A. A. Kiselev, I. Alvarado-Rodriguez, R. S. Ross, A. E. Schmitz, M. Sokolich, C. A. Watson, M. F. Gyure, and A. T. Hunter, Nature (London) **481**, 344 (2012).
[48] J. R. Petta, A. C. Johnson, J. M. Taylor, E. A. Laird, A. Yacoby, M. D. Lukin, C. M. Marcus, M. P. Hanson, and A. C. Gossard, Science **309**, 2180 (2005).